J Appl Physiol 110: 943–955, 2011.
First published February 3, 2011; doi:10.1152/japplphysiol.00775.2010.

The interdependent contributions of gravitational and structural features to perfusion distribution in a multiscale model of the pulmonary circulation

A. R. Clark,[1] M. H. Tawhai,[1] E. A. Hoffman,[2] and K. S. Burrowes[3]

[1]*Auckland Bioengineering Institute, University of Auckland, Auckland, New Zealand;* [2]*Departments of Radiology and Biomedical Engineering, University of Iowa, Iowa City, Iowa; and* [3]*Oxford University Computing Laboratory, University of Oxford, Oxford, United Kingdom*

Submitted 8 July 2010; accepted in final form 28 January 2011

Clark AR, Tawhai MH, Hoffman EA, Burrowes KS. The interdependent contributions of gravitational and structural features to perfusion distribution in a multiscale model of the pulmonary circulation. *J Appl Physiol* 110: 943–955, 2011. First published February 3, 2011; doi:10.1152/japplphysiol.00775.2010.—Recent experimental and imaging studies suggest that the influence of gravity on the measured distribution of blood flow in the lung is largely through deformation of the parenchymal tissue. To study the contribution of hydrostatic effects to regional perfusion in the presence of tissue deformation, we have developed an anatomically structured computational model of the pulmonary circulation (arteries, capillaries, veins), coupled to a continuum model of tissue deformation, and including scale-appropriate fluid dynamics for blood flow in each vessel type. The model demonstrates that both structural and the multiple effects of gravity on the pulmonary circulation make a distinct contribution to the distribution of blood. It shows that postural differences in perfusion gradients can be explained by the combined effect of tissue deformation and extra-acinar blood vessel resistance to flow in the dependent tissue. However, gravitational perfusion gradients persist when the effect of tissue deformation is eliminated, highlighting the importance of the hydrostatic effects of gravity on blood distribution in the pulmonary circulation. Coupling of large- and small-scale models reveals variation in microcirculatory driving pressures within isogravitational planes due to extra-acinar vessel resistance. Variation in driving pressures is due to heterogeneous large-vessel resistance as a consequence of geometric asymmetry in the vascular trees and is amplified by the complex balance of pressures, distension, and flow at the microcirculatory level.

pulmonary blood flow; modeling; flow heterogeneity

THE FUNCTION OF THE BLOOD transport system in the lung is dependent on the lung's material properties and the resultant mechanical deformation of the parenchymal tissue to which the vascular transport trees are tethered. Lung tissue can be described as acting as a "Slinky" that deforms under gravity, resulting in a gravitational gradient in parenchymal tissue density with relatively compressed tissue in gravitationally dependent lung regions (35, 48). Recent experimental and imaging studies have highlighted the effect of gravity acting to deform the parenchymal tissue (35, 46, 48) on the regional distribution of blood flow in the lung, in addition to the balance of hydrostatic pressures at the microcirculatory level, as described by the classic "zonal" model for pulmonary perfusion (59). The anatomical geometry of the lung and vasculature have also been proposed to be important contributors to pulmonary perfusion distribution (25, 31). However, the relative contribution of each of these mechanisms is not clear, because experimental studies cannot separate the effects of vascular branching geometry from the multiple (potentially compound) influences of gravity, including deformation of the tissue and the hydrostatic effect of gravity acting directly on blood. Computational models of the pulmonary circulation allow control over these multiple influences via parameter manipulation. A computational model that uses known physiological principles to represent each of *1*) an anatomically based lung shape and vascular branching geometry, *2*) the microcirculation, *3*) the mechanical interaction between gravity and lung tissue, and *4*) the hydrostatic effect of gravity acting directly on the blood has the potential to elucidate the relative importance of each contributing factor to regional blood flow distribution in the lung.

The complexity of the pulmonary circulation means that theoretical models must necessarily neglect some structural or functional aspects that could contribute to perfusion distribution. Early models of the whole pulmonary circulation used simplified (generally symmetric) large-vessel (arterial and venous) structures, which were joined at their terminal branches by "sheets" representing the capillary vessels (6, 38, 42, 61, 62). More recently, anatomically based representations of extra-acinar arterial and venous structures have been developed, and equations representing blood flow have been solved to predict perfusion distribution within these structures (7, 8, 11, 13). Computational constraints have so far prevented these anatomically structured models of blood flow in the arterial and venous trees from being coupled via models of blood flow in the small vessels that join the two structures (the intra-acinar blood vessels), and so pressure or flow boundary conditions must be assumed at the level of the acinus to acquire a solution. Perfusion of the pulmonary capillaries has also been modeled, both with capillary perfusion represented as flow through a sheet (18) and through more computationally expensive, but anatomically accurate, networks of tubules (12, 40). Each of these scales of model is able to capture some important features of pulmonary perfusion distribution, but structural simplifications in precapillary vessels (6, 38, 42, 61, 62), or assumptions made regarding boundary conditions (7, 8, 11, 13) restrict their predictive power with regard to perfusion gradients and heterogeneity.

Here we present an anatomically based model of blood flow through the full pulmonary circuit of a single human subject, coupled to a model of parenchymal tissue mechanics (53), to study the interdependence of structure, fluid transport, and mechanical behavior in perfusion of the lung. This study specifically addresses whether tissue deformation is the major contribution of gravity to the pulmonary perfusion gradient in

Address for reprint requests and other correspondence: A. Clark, Auckland Bioengineering Institute, Univ. of Auckland, Private Bag 92019, Auckland Mail Centre, Auckland 1142, New Zealand (e-mail: alys.clark@auckland.ac.nz).

the human lung, whether the hydrostatic pressure gradient makes a quantifiable contribution, and whether the balance of pressures at the microcirculatory level remains a significant feature in the presence of other mechanisms of gravitational origin. This modeling framework builds on our laboratory's previous work (7, 8, 11, 13) by coupling anatomically based preacinar geometries (representing the largest pulmonary arteries and veins) with a recently developed "ladder" model of perfusion in the pulmonary acinus (14), which represents the capillaries as sheets (18) and includes intra-acinar vessels.

METHODS

Model Geometry

The model geometry presented here is anatomically based, in that it captures aspects of the branching asymmetry of the extra-acinar pulmonary blood vessels and the spatial relationship between blood vessels and lung parenchymal tissue. It is subject specific to the extent that it describes the lung shape, the distribution of the largest blood vessels, and the regional tissue density (ρ_t) measured from multirow detector computed tomography (MDCT) data in an individual. Where subject-specific data are not available from MDCT data, the modeling methodology aims to capture a structure that corresponds as closely as possible to published data in human subjects.

The geometry of the lung surface, central airways, and the largest pulmonary arteries and veins were derived from MDCT data. MDCT data were acquired at the University of Iowa Comprehensive Lung Imaging Center within the framework of the human lung atlas database (32, 33). The human lung atlas contains image data for human subjects spanning 4 decades of age range. Imaging of all subjects in the database has been approved by the University of Iowa Institutional Review Board and Radiation Safety Committees. Lung volume was controlled by a custom-built (University of Iowa) pneumotachometer-based lung volume control device. Images were acquired using a Siemens Sensation 64 MDCT scanner. The images used in the present study were from a healthy man (age: 25 yr, weight: 90.9 kg, height: 1.90 m) and consisted of a spiral scan of the full lung in the supine posture with inflation level held at 95% vital capacity [assumed here to be representative of total lung capacity (TLC)] and at functional residual capacity (FRC). Scan parameters were: 120 kV, 100 mA, a pitch of 1.2, slice width 0.6 mm, and slice interval 0.6 mm. Lung volumes for this subject measured in the seated position were 4.47 and 8.47 liters at FRC and TLC, respectively. This is the same subject used in the modeling studies of Tawhai et al. (53) and Burrowes and Tawhai (13).

Large (extra-acinar) blood vessels. Each extra-acinar blood vessel was defined using a one-dimensional (1D) finite element, representing its centerline plus a numeric value for its unstrained [zero transmural pressure (Ptm)] radius. Therefore, a blood vessel (or vessel segment) is described by a vector (its centerline), which places it spatially within the lung structure, and its radius. The vector representing the vessel centerline is defined to be in the direction of flow and so begins at the inlet to each vessel and ends at the vessel outlet. This 1D approach assumes vessels to be approximately cylindrical when unstrained, which differs from a three-dimensional (3D) approach, which explicitly describes the volume of each vessel. Although 3D models provide an accurate description of fluid transport, they are not considered here, as they are computationally intensive and are currently not able to describe perfusion in a whole lung structure.

The geometries of the large arteries and veins were modeled using a combination of MDCT data and computational algorithms, as described in detailed in Refs. 8, 52, and 53. The centerlines of the largest blood vessels (main, left, and right pulmonary arteries) were manually segmented from the subject's MDCT data. Each of these blood vessels was represented in the model by multiple 1D finite elements, which reflect the spatial distribution and curvature of the large blood vessels.

Automated image segmentation methods are not yet capable of reliable separation of, and differentiation between, the pulmonary arteries and veins. Because of this constraint, the (subject-specific) centerlines of the central airways obtained from MDCT data were used to construct approximately four generations of the arterial and venous trees distal to the left and right pulmonary arteries and veins. Using the airway tree to construct the blood vessel geometry at this level is a reasonable approximation, as the airways and blood vessels have very similar lengths and orientations: the pulmonary arteries closely follow the airways, and the veins divide at the midpoint between neighboring airway bifurcations (56). This airway centerline data plus the centerline data of the main, left, and right pulmonary vessels provided a 1D finite-element description of the pulmonary blood vessels down to *generations 6–9*.

Finally, the 1D finite-element tree obtained from MDCT data, as described above, was used as an initial condition for generating a tree structure within the subject's lung volume. The methodology for obtaining volumetric meshes from MDCT data, as well as the detail of the volume-filling algorithm used to create the vessel tree structure, are given in previous studies (8, 52). The branching algorithm is deterministic and designed to generate a branching structure that matches as closely as possible morphometric data on vessel lengths and branching angles (see Refs. 8 and 52 for details). The imaged lung volume (including tissue and air) and the seed point density of acinar units [~30,000 acini (30)] in the lung are input parameters. The blood vessel models were generated to represent all accompanying (non-supernumerary) arteries and veins, down to the level of the vessels that accompany the terminal bronchiole in the airway tree (that is, each terminal vessel supplies a single acinus) with each artery and vein represented by a single 1D finite element.

Small (intra-acinar) blood vessels. Each acinar circulatory "unit" is subtended by a single artery and a single vein that accompany a unique terminal bronchiole. Within each unit, the intra-acinar arterioles and venules were explicitly represented, with nine symmetric bifurcations of each type of vessel included in the model (30). These intra-acinar vessels were assumed to be joined at each generation by a capillary bed that covers the alveoli present at that generation, forming a "ladder-like" structure, as previously described by Clark et al. (14).

The capillary bed was represented using the lumped parameter "sheet-flow" model, developed by Fung and Sobin (18). The blood pressure at the midpoint of each arteriole and venule generation was assumed to be a good approximation to the average pressures into and out of pre- and postcapillary vessels arising from this generation. The midpoint of each arteriolar branch was joined to its corresponding venule branch by a capillary sheet, where each connection represents the capillary bed over multiple alveoli (with ~10–15 alveoli per sheet) and may have several feeding precapillary vessels; the small precapillary vessels that do not follow the branching structure of the larger arterioles and venules and have diameters approaching those of the capillary vessels were incorporated into the capillary sheet for modeling purposes. Detail of this intra-acinar model is given by Clark et al. (14).

Vessel dimensions. The diameters of the left pulmonary artery (14.80 mm) and right pulmonary vein (12.97 mm) were assigned based on measurements made by Huang et al. (39) at zero Ptm and close to TLC. These diameters compare well to those given for the same order of vessel in other morphometric studies (36, 50). All other arteries and veins down to the level of the acinus were assigned diameters based on a constant rate of increase in diameter with vessel order (the Strahler diameter ratio R_DS). Conventional Strahler ordering was used to classify vessels in the model (36, 50), with each peripheral vessel (distal-most arteriole or venule) defined as order 1, and a parent vessel being the same order as the child branch of the highest order, or else one order higher than two child branches of the same order.

As a range of values for R_DS exist in the literature, R_DS for the arteries and the veins were treated as fit parameters, such that the model gave physiologically realistic predictions for pulmonary vascular resistance (PVR) in the supine posture at FRC. The fitted R_DS

were 1.53 in the arterial tree and 1.54 in the venous tree. This compares with 1.56 ± 0.02 (arteries) and 1.58 ± 0.06 (veins) calculated from the raw human data of Ref. 39 (where diameter-defined Strahler ordering was used), and 1.56 ± 0.09 (arteries) and 1.61 ± 0.13 (veins) calculated from the raw human data of Refs. 36 and 50 (where conventional Strahler ordering was used).

In the absence of data providing diameter information per generation within the acinus, the diameters of intra-acinar arterioles and venules were assumed to decrease linearly with generation from the diameter value at the level of the terminal bronchiole to the level of Strahler order 1 arterioles and venules, as measured by Huang et al. (39) (0.020 and 0.018 mm, respectively). Similarly, the lengths of intra-acinar vessels were assumed to decrease linearly with generation from the length value in the generated large vessel tree to the level of Strahler order 1 arterioles and venules, as measured by Huang et al. (0.22 and 0.13 mm, respectively).

Tissue Deformation

The extra- and intra-acinar vessels are affected differently by lung inflation (37). Extra-acinar vessels, which are embedded within and tethered to the parenchymal tissue, are distended axially and radially on inflation, resulting in a decrease in resistance. In contrast, alveolar vessels wrap over the surface of the alveoli; therefore, during inflation, they are stretched axially but compressed radially. This leads to an increase in resistance in the vessels on inflation. These opposing effects result in a minimum for PVR at approximately FRC and increasing resistance for larger or smaller lung volumes (54). As imaging data and reference vessel dimensions were obtained at, or close to, TLC volume, the effect of deflation from TLC to FRC was modeled, as described below.

Finite deformation elasticity. The extra-acinar vascular models were coupled to a soft tissue mechanics model, which calculates local volume changes of the lung due to gravity and lung expansion (13, 53). In brief, the soft tissue mechanics model assumes the lung-air matrix to be a compressible, nonlinearly elastic continuum with homogeneous and isotropic material properties. The lung is free to slide within a rigid "pleural" body. Contact between the surfaces of the lung and pleural body are enforced using frictionless contact constraints.

To represent different postures and volumes, deformation of the lung was predicted using the soft tissue mechanics model, for a change in volume of the pleural body from FRC to TLC under a given direction of gravity. The vascular model was embedded within the lung volume and deformed with the tissue. The distribution of ρ_t (including all lung tissue, blood, and extravascular water), elastic recoil pressures (P_e), and deformation of the arterial and venous meshes were then calculated. At FRC, the ρ_t (validated against MDCT data) and P_e distributions are gravitationally dependent with the largest variation in each occurring in the supine position (compared with prone and upright). These distributions are discussed in detail in previous publications (13, 53).

Coupling tissue mechanics to blood flow. The effect of axial and radial tissue tethering to extra-acinar blood vessels was incorporated into the model, as described in detail by Ref. 13. A "stretch factor" (λ, the ratio of deformed to TLC length) was calculated for each vessel based on the deformation of the mechanics model. Vessel length (L) and diameter (D_0) were then defined using

$$L = \lambda L^*, \quad D_0 = D_0^* \sqrt{\frac{1}{\lambda}}$$

where L^* is the vessel length at TLC, and D_0^* is the unstrained (Ptm = 0) vessel diameter at TLC. This assumes conservation of blood volume between TLC and FRC in the extra-acinar vessels. The MDCT data for this subject show a marginal (3.6%) decrease in total tissue (including blood) volume between TLC and FRC. If this difference were entirely due to a decrease in blood volume (spread evenly between all vessels), it would result in a 1.8% increase in the stretch factor compared with when conservation of blood volume is assumed. The mean decrease in tissue volume between TLC and FRC over 43 normal subjects from the human lung atlas database was 2.9% (standard deviation 5.7%; several subjects showed an increase in tissue volume). This mean value would result in a 1.5% increase in the stretch factor, which does not significantly affect results.

Radial deformation of the extracapillary (both extra- and intra-acinar) blood vessels was also related to Ptm by an approximately linear relationship

$$\frac{D}{D_0} = \alpha P_{tm} + 1 \qquad (1)$$

where D is the strained vessel diameter, and α is a compliance constant (42). It was assumed that the tethering pressure acting radially on a blood vessel was equal and opposite to the local P_e, and so, in these large blood vessels, Ptm $\approx P_b - P_e$ (where P_b is the average blood pressure across the length of the vessel). *Equation 1* also holds for the acinar arterioles and venules. However, in the smallest arterioles and venules (with diameter <200 μm), the dominant pressure acting externally to the blood vessel is likely to be alveolar pressure (P_A), and so in these vessels Ptm $\approx P_b - P_A$ was used (60).

The thickness of the capillary sheet (H) can be expressed via an equation similar to *Equation 1* as

$$\frac{H}{H_0} = \alpha_C P_{tm} + 1 \qquad (2)$$

where H_0 is the unstrained capillary sheet thickness, α_c is a compliance constant for the capillary sheet, and Ptm $\approx P_b - P_A$ (17). *Equations 1* and *2* were assumed to be valid up to a maximum Ptm of 32 cmH_2O (3.1 kPa) (51), beyond which the vessel was assumed to be maximally extended in the radial direction.

On inflation, alveoli become expanded, causing the capillaries to lengthen. This lengthening results in an effective reduction in capillary compliance (α_C) with increasing transpulmonary pressure (Ptp). Glazier et al. (21) measured capillary sheet height and compliance in dog lungs at two different lung volumes roughly equivalent to FRC (α_C = 0.122 μm/cmH_2O, Ptp = 4 cmH_2O) and TLC (α_C = 0.079 μm/cmH_2O, Ptp = 25 cmH_2O). Here we assumed that α_C is a linear function of Ptp

$$\alpha_C(P_{tp}) = a + bP_{tp}$$

where a and b are constants, and Ptp is assumed to be equal and opposite to local P_e. The constants a and b are first calculated for dogs from the data of Glazier et al. (21) [a = 0.130 μm/cmH_2O and $b = -2.04 \times 10^{-3}$ μm/$(cmH_2O)^2$]. Then, using a measured value for α_C in humans of 0.127 μm/cmH_2O (16) and assuming that this value was attained midway between FRC and TLC (Ptp = 14.5 cmH_2O), the constants were scaled to be a = 0.165 μm/cmH_2O and $b = -2.58 \times 10^{-3}$ μm/$(cmH_2O)^2$.

Blood Flow Models

Blood flow in each element of the model geometry was calculated depending on the "vessel type" classification of the vessel in question (artery, vein, arteriole, venule, or capillary).

Blood flow in the extra-acinar vessels was described by a Poiseuille equation incorporating the effect of gravity acting on the blood in the direction of the vessel centerline. Thus flow in an artery or vein was described by

$$\Delta P = \frac{128\mu L}{\pi D^4}\dot{Q} + \rho_b g L \cos\Theta \qquad (3)$$

where ΔP is the pressure drop along the vessel, μ is the viscosity of blood in the vessel, $\dot{Q}$ is the volumetric blood flow rate, ρ_b is the blood

density in the vessel, g represents gravitational acceleration (9.81 m/s^2), and Θ is the angle that the vector along the centerline of the blood vessel makes with the direction of gravity. The gravity vector is oriented either along the dorsoventral axis (prone and supine postures) or the craniocaudal axis (upright). This 1D model assumes that flow dominates along the centerline of the vessel.

The length of acinar arterioles and venules was assumed to be sufficiently small that the effect of gravity on these vessels was negligible. Therefore, flow in the arterioles and venules was described by Poiseuille's equation

$$\Delta P = \frac{128\mu L}{\pi D^4}\dot{Q} \quad (4)$$

Finally, blood flow in a capillary sheet is described using the sheet flow model of Fung and Sobin (18)

$$\dot{Q} = \frac{SA}{\mu_C f l_C^2}\int H^3 dP_{tm} \quad (5)$$

where S is the proportion of alveolar surface area comprised of capillaries, A is alveolar surface area, μ_C is the apparent viscosity of blood in the capillaries, f is a numerical friction factor, and l_C is the average pathlength from an arteriole to a venule through the capillary network. Explicit calculation of the integral term in this equation is given in Appendix A of Ref.14.

Capillary Recruitment

Classic sheet flow theory accounts for recruitment of capillary blood volume via vessel distension (a pressure-dependent sheet height) plus direct recruitment of blood vessels (on a septa-by-septa basis) when transitioning from West's zone 2 conditions: when venous blood pressure is lower than alveolar air pressure. In this case, Fung and Yen (19) proposed a scaling of capillary surface area under zone 2 conditions, which was dependent on venous side Ptm. This scaling is described in detail in Ref. 14 and relies on cat data for its parameterization.

In addition to zone 2 conditions, there is a substantial portion of the capillary bed that is unperfused under normal respiratory conditions. The mechanism of this is unclear, although it has been proposed that some capillaries have a higher opening pressure than others (43). Using anatomic estimates for capillary surface area (the product SA in *Eq. 5*) would overestimate capillary volume and not allow for a reserve capillary capacity when the lung is under stress; this was not accounted for in the sheet flow model. Therefore, a simple model of capillary recruitment under normal flow (zone 3) conditions was incorporated; to be compatible with sheet flow theory, this model assumes that capillary vessels are recruited regionally on a spatial scale that incorporates multiple capillary vessels (so recruitment is not vessel by vessel). This certainly occurs at low positive airway pressure, is apparently dependent on lung inflation, and is not conclusively known (28, 55).

Godbey et al. (28) measured the percentage of capillary pathways perfused in five dog lungs with intact thorax, perfused over a range of capillary pressures (Fig. 2 in that study). The data from that study obtained at zero airway pressure was used, and the proportion of capillary bed perfused (p_{cap}) is assumed to be a function of the form

$$p_{cap} = 1 - F_{rec}\exp(-P_{cap}^2/\sigma_{rec}^2) \quad (6)$$

where P_{cap} is capillary blood pressure (here taken to be the average of arterial and venous side blood pressure). The constants F_{rec} and σ_{rec} were fitted to the raw data of Ref. 28 using the method of least squares, resulting in $F_{rec} = 0.65$ and $\sigma_{rec} = 22.7$ cmH_2O (2.23 kPa). The capillary surface area in *Eq. 5* was scaled by p_{cap} in the flow and pressure calculations. As zero airway pressure data were used to fit the parameters of *Eq. 6*, this equation may not be valid for applications such as the modeling of perfusion during positive end-expiratory pressure ventilation, when P_A may differ considerably from zero.

Model Solution

An initial estimate was made for the resistance terms in *Eqs. 3*, *4*, and *5* for each vessel within the pulmonary circuit. These equations, along with conservation of mass at each bifurcation (that is $\sum\dot{Q} = 0$ at each bifurcation) form a linear system that was solved to predict the $\dot{Q}$ and P_b distribution throughout the full network. Vessel diameters, capillary heights, and capillary surface area were then updated using *Eqs. 1*, *2*, and *6* and the solution for P_b. These updated vessel dimensions were used to update the resistance terms in *Eqs. 3*, *4*, and *5*. This process was repeated iteratively until convergence was achieved. The convergence criterion was that the sum of squared differences for all values of $\dot{Q}$, P_b, and D was $<10^{-8}$. In this study, a flow boundary condition into the inlet artery (cardiac output) of 5 l/min was imposed along with a left atrial pressure of 5 mmHg (6.67 kPa). This allowed calculation of pulmonary artery pressure and PVR. Model solutions were obtained at FRC in each of the prone, supine, and upright postures.

Calculation of Perfusion Gradients and Solution Analysis

Calculation of perfusion gradients and coefficients of variation [COVs; equivalent to relative dispersion (RD)] varies considerably in experimental studies, and the values of these measures depend on the method of image processing and analysis employed in the study (i.e., image resolution, edge exclusion criteria, etc.). Here we calculated perfusion gradients and COVs on both a per-voxel and a per-acinus basis.

Per-voxel analysis. For per-voxel analyses, the lung was divided into a number of equally sized cubes (or voxels) of 1 cm^3. Flows to acini within each voxel were then summed before calculation of gradients and COVs. Voxels were omitted from analysis if they lay on the surface of the lung and were only partially filled with lung tissue (edges were excluded). If a finite element representing an acinus lay on the boundary between voxels, it was assigned to only one of the voxels. This analysis technique aims to mimic imaging measures using radiolabeled macroaggregates that become lodged in the small blood vessels that comprise the parenchymal tissue (46). A per-voxel analysis mimicking image-based voxel measurements, such as functional MRI, that included all blood vessels (as well as acinar units) was also carried out, as detailed in the APPENDIX. An example of this type of study is that of Prisk et al. (48), although the results presented here are only directly comparable to the results in that study, which do not include a density normalization. Results from this additional analysis differ only slightly from the results we present in Fig. 1 (discussed below).

Per-acinus analysis. The model described here predicts a blood flow rate into each distinct acinar unit. Using the spatial location of each acinar unit, a per tissue unit volume description of blood flow gradients and COVs are obtained. This illustrates the regional distribution of blood flow that would be obtained if every acinar unit in the model were adjusted to an identical unstressed volume. All acinar units are included in this analysis as an individual data point, including those acinar units near the edge of the lung. This provides results that are comparable to blood flow measurements made in animals using microsphere injection, where intravascular microsphere deposition is normalized by blood-free dried tissue weight (25).

In each of the per-voxel and per-acinus analyses, gradients of blood flow with respect to gravitational height were calculated using a linear regression analysis. Flow in each voxel (or acinus) was regressed against gravitational height. The COV (overall standard deviation divided by the mean flow) was calculated as a measure of flow heterogeneity. Here the mean flow was calculated as the sum of the flow through all voxels (or acini) divided by the number of voxels (or acini).

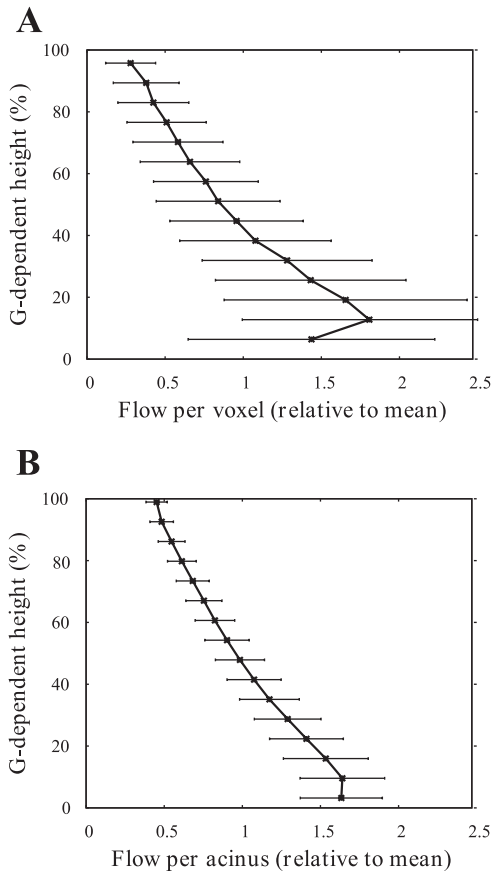

Fig. 1. Blood flow per 1-cm^3 voxel (*A*) and per acinus (*B*) averaged within 10-mm isogravitational planes and plotted as a function of percentage of gravitational height. Each flow value is divided by the mean flow per voxel (*A*) or acinus (*B*) over the whole lung to allow comparison between the two analysis techniques considered. Error bars represent 1 SD. Results are shown at functional residual capacity (FRC) in the supine posture. The per-voxel plot (*A*) appears to cover less of the lung than the per-acinus plots (*B*), as "edge" voxels are excluded from analysis. Comparisons between blood flow distributions between postures are given in Fig. 2.

RESULTS

Table 1 summarizes model predictions of pulmonary artery pressure, PVR, perfusion gradients, and COV at FRC in the prone, supine, and upright positions. Blood flow in the per-voxel analysis (Table 1, *columns 4* and *5*) was not normalized by ρ_t (as is often the case in experimental studies, providing a correction for tissue deformation). As we include only acinar units in our per-voxel analysis, we can determine the number of acini in each voxel exactly. Dividing flows in each voxel by the number of acini in that voxel provides a density normalized approximation. Perfusion gradients normalized in this manner and calculated with progressively smaller voxel sizes tend to the gradients calculated on a per-acinus basis. Therefore, the per-acinus analysis included here provides prediction of density-normalized perfusion (Table 1, *columns 6* and *7*).

Variability in perfusion with gravitational height in the supine posture at FRC is illustrated in Fig. 1 using both the per-voxel and per-acinus analysis techniques described above. The mean and standard deviation of blood flow calculated within 10-mm isogravitational slices is shown. Here the mean flow was calculated as the sum of the flow through all voxels (acini) divided by the number of voxels (acini). The model predicts a heterogeneous perfusion distribution within isogravitational slices [as illustrated by the error bars (±SD) in Fig. 1], increasing blood flow down most of the gravitational height of the lung, and a section of decreasing flow in the most gravitationally dependent lung region (classified as "zone 4" flow).

Figure 2 compares mean flow in 10-mm-thick slices of the lung in each of the prone, supine, and upright postures obtained via per-voxel and per-acinus analysis. On a per-acinus basis (so with density normalization), the change in flow with gravitational height in nonzone 4 regions is almost identical for each posture (Fig. 2*B*). Without density normalization (the per-voxel analysis, Fig. 2*A*), there is still considerable similarity between gradients, but this similarity is less evident than in the per-acinus analysis.

The presence of zone 4 and the relative size of this region in each posture skews predicted flow gradients. Therefore, perfusion gradients were recalculated on a per-acinus basis (so effectively density normalized) and excluding zone 4. Zone 4 was excluded by removal of acini in the lower 15% of the lung height (with respect to gravity) so that the acini that lie in the most dependent region of lung tissue are excluded from analysis. The per-acinus perfusion gradients excluding zone 4 were −7.78, −7.59, and −7.57%/cm in the prone, supine, and upright postures, respectively. These values are remarkably similar compared with the gradients for each posture in Table 1, suggesting that differences between perfusion gradients in different postures, although not the gradients themselves, can be eliminated by density normalization and removal of zone 4 regions.

As illustrated in Fig. 1, perfusion is heterogeneous within isogravitational slices of the lung. In the model, this heterogeneity is consistent with heterogeneity in acinar-level driving pressures. Figure 3 shows the blood pressure drop that occurs across the acinus plotted against gravitational height (Fig. 3*A*), and upstream (arterial) resistance plotted against the pressure

Table 1. *Model predictions of PAP, PVR, G (including zone 4 regions), and COV in each posture at FRC*

	Mean PAP, kPa (mmHg)	PVR, dyn·s·cm^{-5}	Per Voxel		Per Acinus	
			G, %/cm	COV, %	G, %/cm	COV, %
Supine	2.43 (18.2)	212	−11.7 (R^2 = 0.46)	60.7	−7.91 (R^2 = 0.71)	34.6
Prone	2.24 (16.8)	189	−10.0 (R^2 = 0.37)	53.9	−8.14 (R^2 = 0.74)	37.7
Upright	2.10 (15.8)	172	−5.19 (R^2 = 0.27)	51.9	−7.76 (R^2 = 0.82)	42.8
Literature values	2.00 (15)	<240 (Ref. 49)	−1.1 to −11 (Refs. 3, 35, 45, 46, 48)	69–78 (Refs. 35, 48)	N/A	N/A

FRC, functional residual capacity; PAP, pulmonary arterial pressure; PVR, pulmonary vascular resistance; G, perfusion gradients; COV, coefficient of variation; N/A, not applicable. PAP values are given in kPa (with mmHg values in parentheses). G and COV are calculated using each of the common analysis techniques described in the main text of this paper.

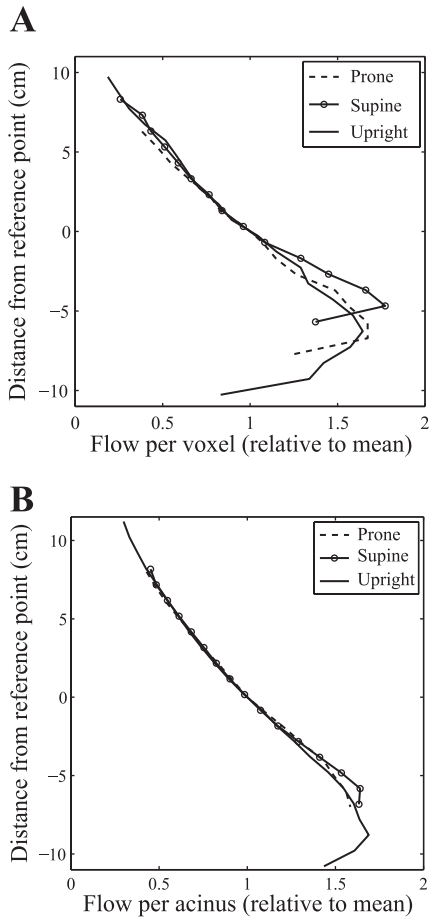

Fig. 2. Blood flow per 1-cm^3 voxel (*A*) and per acinus (*B*) averaged within 10-mm isogravitational planes and plotted as a function of distance from a reference height in each of the supine, prone, and upright postures at FRC. Each flow value is divided by the mean flow per voxel (*A*) or acinus (*B*) over the whole lung. To allow comparison between postures, the reference height is chosen to be the point closest to the center of the lung (in the direction of gravity) at which the flow value equals the mean flow per voxel or per acinus. Therefore, each curve intercepts at the point (1,0).

drop across the acinus (Fig. 3*B*) in the supine posture. There is a clear (close to linear) relationship between upstream resistance and acinar driving pressure across postures, with gradients of -0.03, -0.03, and -0.04 mm^3·Pa^{-1}·s^{-1} and R^2 = 0.85, 0.85, and 0.89 in the prone, supine, and upright postures, respectively. The resistance upstream from the acinus has a major influence on the acinar driving pressure. This is a consequence of the anatomic branching structure, which results in variable pathlengths from the main pulmonary artery to the gas exchange surface.

Table 1 shows that predicted COVs are lower when calculated on a per-acinus basis than on a per-voxel basis. Calculating COV on a per-voxel basis with approximately acinus-sized voxels (~140 mm^3) results in values of 69.7, 69.6, and 65.6% in the supine, prone, and upright postures, respectively. It is expected that the COV calculated on a per-acinus basis will be lower than that calculated on a per-voxel basis: even when voxels are approximately the size of an acinus, some will contain more acini than others (due to the nonuniform distribution of acini within the lung), and so heterogeneity between voxels will be higher than between individual acini. Although edge voxels were omitted from analysis, voxels that contain several large blood vessels and so fewer acini were not. This means that, over the whole lung, the COV of the number of acini per voxel is 37%, which provides a possible explanation for the observed difference. Figure 4 shows the logarithm of COV calculated on a per-voxel basis plotted as a function of the logarithm of voxel size. This model prediction is comparable to data obtained from dog lungs (27), also shown in Fig. 4. Model predictions and experimental data show COV increasing with decreasing voxel size over most of the range of voxel sizes considered, and the log-log relationship is approximately linear within this range.

A sensitivity analysis for model parameters is given in Table 2. Model predictions of PVR are most sensitive to parameters relating to vessel dimension; that is, vessel radius and compliance. It is clear that any change in vessel compliance (e.g., due to lung disease) or vessel constriction and dilation would have a significant effect on PVR and blood flow distribution. Although PVR is sensitive to inlet vessel radii, it should be noted that, following the simulations, the strained radii of the largest pulmonary vessels were compared with the computed tomography (CT) images of the subject in question and matched well.

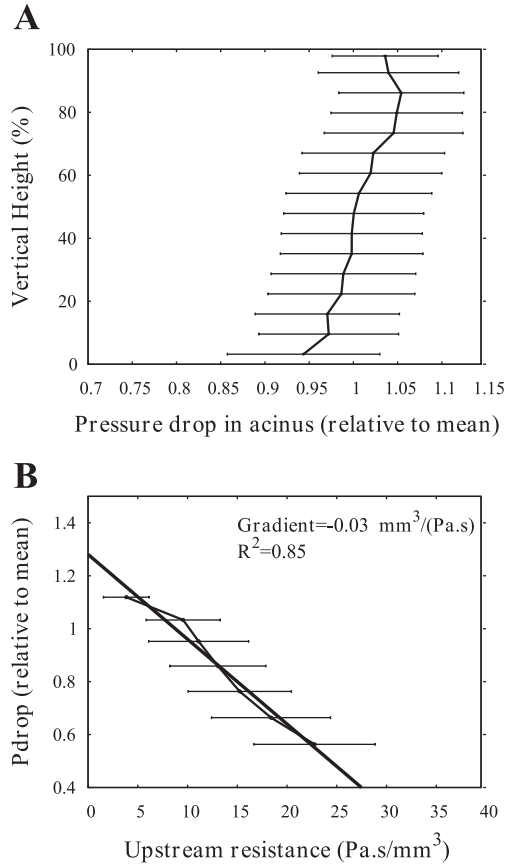

Fig. 3. *A*: the pressure drop (Pdrop) across each acinus averaged within 10-mm isogravitational planes and plotted as a function of percentage of gravitational height. Each Pdrop is divided by the mean Pdrop across all acini (the sum of the Pdrop values across each individual acinus divided by the number of acini), and error bars represent 1 SD within isogravitational planes. *B*: the Pdrop across each acinus plotted as a function of upstream (preacinar, arterial) resistance (Pa·s^{-1}·mm^{-3}). Again, each Pdrop is divided by the mean Pdrop across all acini, and error bars represent 1 SD in the resistance. Results are shown at FRC in the supine posture.

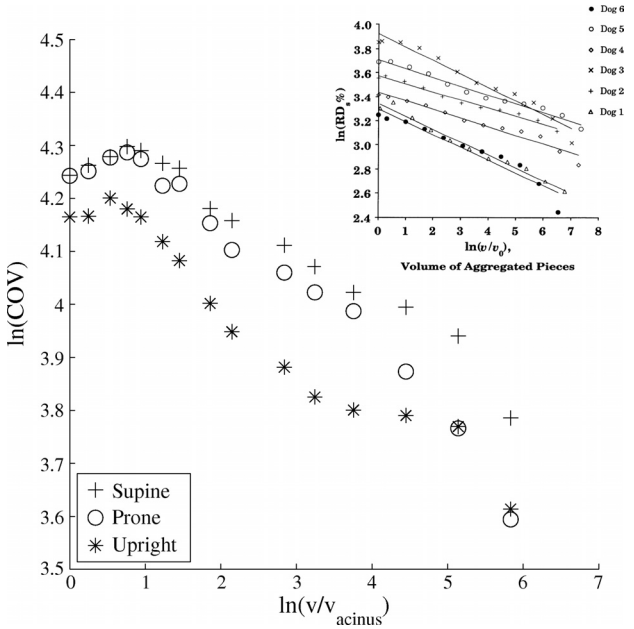

Fig. 4. The logarithm of coefficient of variation (COV; %) at FRC as obtained via a per-voxel analysis of model predictions plotted as a function of the logarithm of voxel volume (v). The smallest voxels considered are approximately the volume of an acinus (v_{acinus} = FRC lung volume/number of acini). *Inset* (adapted from Ref. 26): similar results obtained experimentally from 6 dog lungs in the supine posture. RD, relative dispersion.

This provided some validation of the choice of vessel radii incorporated into the model. In general, flow gradients are less sensitive to perfusion model parameters than PVR, suggesting that the major contributors to these gradients are anatomic structure, tissue deformation, and the weight of the blood. An analysis of the sensitivity of model predictions to boundary conditions (left atrial pressure and cardiac output) was also carried out. Altering the two parameters by ±10% from baseline does not have a major effect on model predictions of perfusion distribution and PVR. However, it should be noted that an increase in cardiac output reduces the predicted perfusion gradient due to a redistribution of predicted flows to nondependent lung regions (regions in which there is the most capacity for recruitment of capillary volume at baseline).

The effect of gravitational factors on predicted perfusion gradients and COV (including all acini in the lung) was assessed in the supine model at FRC by "switching off" each of the gravitational influences one at a time. The model was solved in *1*) zero gravity conditions (0 G), assuming a uniform expansion of the lung between FRC and TLC (no tissue deformation); *2*) with no tissue deformation, but including the effect of hydrostatic pressure on blood ($\rho_b\ gL\ \cos\Theta$ in *Eq. 3* and "zonal" flow in the capillary model); and *3*) with no hydrostatic pressure effects, but including tissue deformation. Results are shown in Table 3 as a percent change from baseline model predictions (as shown in Table 1) in the supine posture at FRC. The vascular branching asymmetry contributes little to the perfusion gradient; however, it is a major contributor to flow heterogeneity, with a large proportion of the COV predicted in the full model evident in 0-G simulations. The branching structure is also responsible for regions of reduced flow in the peripheral lung, where longer pathlengths exist. The combination of these longer pathlengths and gravity induce the zone 4 flow regions typically found in the dependent lung tissue. Hydrostatic pressure has a substantial effect on the development of a perfusion gradient, with simulations including this effect alone showing a significant increase in perfusion gradients compared with 0-G simulations. Tissue deformation adds to this effect; simulations with tissue deformation and no hydrostatic effects show a substantial perfusion gradient when flow is not normalized by ρ_t (the per-voxel results in Table 3) and density normalized (per-acinus results) are more similar to 0-G simulations.

DISCUSSION

We have developed a model of pulmonary blood flow coupled to soft tissue mechanics that is anatomically based and includes the full accompanying pulmonary circuit (arteries, arterioles, capillaries, venules, and veins). The model confirms the importance of gravity acting to deform tissue on the magnitude of pulmonary perfusion gradients and observed postural differences between gradients, it shows that the hydrostatic effect of gravity on blood is significant in the development of perfusion gradients, and it accounts for heterogeneity in pulmonary perfusion due to asymmetry in vascular structure.

This model further develops previous modeling attempts designed to investigate perfusion heterogeneity and the influence of gravity on pulmonary perfusion (7, 9, 10, 13), which consider perfusion only in large-vessel structures and rely on assumed blood pressure distributions at the acinar level. This model requires boundary conditions to be specified only at the heart and allows investigation into the influence of both gravity and blood vessel structure on acinar level driving pressures that has not previously been possible via computational modeling. The coupling of models describing the microcirculation with an anatomically based large-vessel structure enables application of readily measurable pressure and/or flow boundary conditions at the heart rather than at the microcirculatory level, as previous anatomically based models have been constrained to do (7, 8, 11, 13).

The modeling approach here includes certain subject-specific features of the lung anatomy and fluid dynamics for the transport of blood, as previously described in the literature. It simultaneously includes a model for the effect of gravity acting on the weight of the lung tissue. Although the model includes subject-specific geometry, its function is designed as a general representation of human lung physiology rather than an attempt to mimic function in the specific individual.

Model Consistency with Measured Physiological Parameters

PVR. The R_DS values that were used to define the diameters of the majority of the arteries and veins were fitted such that the baseline PVR (supine, at FRC) was physiologically reasonable [$<$240 dyn·s·cm^{-5} in healthy individuals (49)]. The model also predicts physiologically reasonable values for PVR at FRC in the prone and upright postures in the single subject considered (Table 1). The predicted PVR increases with lung volume; following inflation from FRC to TLC in the supine posture, the model prediction for PVR increases by 24%. The sensitivity analysis shows small increases in PVR with a 10% increase or decrease in lung volume from FRC. This is consistent with the concept of a minimal PVR at approximately FRC (54). Differ-

Table 2. *A description and sensitivity analysis for model parameters in the supine posture at FRC*

Parameter	Description	Ref. No.	Value	PVR, %		Gradient (Per Acinus), %	
				+10%	−10%	+10%	−10%
			Extracapillary parameters				
α	Vessel compliance	42	1.49×10^{-4} Pa^{-1}	−6.6	+6.2	+3.3	−3.2
μ	Blood viscosity	47	3.36×10^{-3} Pa/s	+3.6	−1.9	−1.3	<1
ρ_b	Blood density	47	1.05×10^{-6} kg/mm^3	+1.2	−1.0	+6.3	−7.0
P_{max}	Pressure at which maximum vessel distension occurs	51	32 cmH_2O	<1	<1	<1	<1
D_0	Left pulmonary artery diameter	See text	14.80 mm	−7.3	+11.3	<1	−1.6
D_0	Right pulmonary vein diameter	See text	12.97 mm	−13.6	+21.9	+2.3	−3.3
	Strahler diameter ratio (arteries)	See text	1.53 (no units)	+10.7	−22.5	−2.1	+4.2
	Strahler diameter ratio (veins)	See text	1.54 (no units)	+21.5	−14.7	−3.0	+2.5
	Cardiac output (CO)	See text	5 l/min	−4.6	−1.0	+5.3	+1.1
	Left atrial pressure (LAP)	See text	5 mmHg	−2.1	<1	−3.2	+1.1
			Capillary parameters				
A	Total capillary sheet area	20	73 m^2 at TLC	−2.9	+3.7	+1.2	<1
α_C	Average sheet compliance	16	1.30×10^{-9} m/Pa	−4.4	+5.3	<1	<1
C	Numerical constant in pressure-alveolar volume relationship	5	0.1 Pa^{-1}	<1	<1	<1	<1
F	Numerical friction factor	17	21.6 (no units)	3.3	−3.3	<1	−1.4
F	Highest proportion of sheet collapse in zone 2	19	0.104 (no units)	<1	<1	<1	<1
F_{rec}	Maximum sheet collapse in normal conditions	See text	0.65 (no units)	1.5	−1.3	+2.5	−2.4
H_0	Unstrained sheet height	16	3.5×10^{-6} m	−4.7	+5.8	−3.4	+3.6
l_C	Average pathlength from arteriole to venule	61	$1,186 \times 10^{-6}$ m at TLC	+6.9	−6.3	+1.9	−2.5
S	The vascular space-to-tissue ratio	20	0.86 (no units)	−2.9	+3.7	+1.2	<1
σ	Numerical constant in zone 2 sheet collapse equation	19	436 Pa	<1	<1	<1	<1
σ_{rec}	Numerical constant in *Eq. 6*	See text	2,230 Pa	+2.1	−2.0	+2.6	−1.1
μ_C	Apparent blood viscosity in capillary beds	16	1.92×10^{-3} Pa/s	+3.3	−3.3	<1	−1.4
	Lung volume	MDCT images	4.47 liters (FRC)	+3.0	<1	−8.7	+7.8

We show the effect of a 10% increase (+10%) or decrease (−10%) in each parameter on PVR and pulmonary perfusion gradients (per acinus). Changes in flow gradient are measured such that a positive change reflects an increase in the steepness of the gradient. A full description of parameters at the capillary level is given in Ref. 14. TLC, total lung capacity; MDCT, multirow detector computed tomography.

ences in PVR between postures are small. However, the lowest PVR is predicted when in the upright posture, and the highest PVR is predicted when supine. This difference may be a result of differing tissue deformation between postures. The model does not incorporate any change in lung shape or volume with posture (the volume and shape are for the supine lung), which may have an influence on predicted PVR when the lung is not supine. Consistency with literature values and trends for PVR provides only a weak, although necessary, validation of the model. Hemodynamic measurements on which an estimate of PVR could be made for this subject were not available.

Perfusion heterogeneity. Perfusion heterogeneity is typically quantified via calculation of the COV. The per-voxel analysis approximates the approach used in human experimental studies; human COV values calculated from MRI data are 75 ± 20% (69 ± 20% when normalized by ρ_t), averaged over prone and supine postures (48), 78 ± 23% in the supine posture, and 72 ± 23% in the prone posture (35, 48). A small reduction in COVs predicted from modeling is expected, as model data are free of noise and are not affected by factors such as partial voluming. Despite this, COVs predicted by our model and calculated on a per-voxel basis are consistent with these estimates (Table 1 and Fig. 4). In addition, predicted COVs are similar between postures (Table 1), which is consistent with the findings of the MRI studies, which found no significant difference between COVs in the prone and supine postures.

Table 1 and Fig. 1 show that both COV values and standard deviations for flow within isogravitational slices of the lung are

Table 3. *Model predictions of altered G and COV in the supine posture at FRC, illustrating the individual and compound effects of hydrostatic pressure and tissue deformation*

	Per Voxel		Per Acinus	
	%Baseline G	%Baseline COV	%Baseline G	%Baseline COV
1) 0 G; no tissue deformation or hydrostatic effects	5.9	74	0.7	47
2) Hydrostatic effects; no tissue deformation	62	84	80	85
3) Tissue deformation; no hydrostatic effects	51	79	23	51

The model is solved in *1*) zero gravity conditions (0 G), assuming a uniform expansion of the lung between FRC and TLC (no tissue deformation); *2*) including the hydrostatic effects of gravity on blood, but with no tissue deformation; and *3*) with no hydrostatic effects of gravity acting directly on the blood, but including the gravitational effects of tissue deformation. Results are shown as a percentage of baseline model predictions in the supine posture at FRC, as shown in Table 1.

considerably higher when flow is averaged over 1-cm^3 voxels than when flow is considered on a per-acinus basis. In the per-voxel analysis, even when voxel size is very small, there is considerable variation in the number of acini (or parts of several acini) residing within individual voxels. As flow is summed within a voxel, this can act to increase heterogeneity between voxels. In some experimental studies, this is accounted for by normalizing flow per voxel by an estimate for the ρ_t in that voxel; this approach shows a small decrease in measured COV in MRI studies compared with a nonnormalized analysis (48). In a microsphere study of six dogs (25), COV was found to be within the range 35–65%; here the number of alveoli in a tissue sample (equivalent to a voxel) was estimated to be proportional to the weight of the tissue sample, as the dog lungs were inflated to TLC before analysis. Our per-acinus values do not require any estimates of ρ_t per voxel or sample and are comparable to values for COV measured by microsphere techniques, which are not conducted in human subjects. For this model of a human subject, the predictions of COV lie at the lower end of the range found experimentally in dogs.

COVs are commonly discussed in the literature with reference to the concept of the lung airways and blood vessels as a pseudofractal (or self-similar) structure (2, 27). Over an appropriate range of spatial scales, the log-log plot of COV and voxel size is expected to be approximately linear, and COV is expected to increase with decreasing voxel size. Figure 4, which shows this log-log plot in each posture considered here, indeed shows a linear relationship in the midrange of voxel sizes considered. For the largest and smallest voxel sizes, the relationship deviates significantly from the linear one that is expected from a fractal structure. At the largest scale, the use of COV as a measure of heterogeneity becomes meaningless: voxels of the size of whole lungs or lobes, for example, are too smoothed to provide information on perfusion heterogeneity within the pulmonary system (2). Of more interest are deviations from the linear relationship when smaller and smaller voxels are considered.

The description of the pulmonary circulation as a pseudofractal system accounts for the fact that pulmonary blood vessels do not divide indefinitely; this means that the log-linear relationship between COV and voxel size cannot continue for very small voxel sizes (2, 27). If voxel sizes continue to be reduced beyond the spatial scale at which perfusion is close to uniform, then theoretically the log-log plot of COV and voxel size would plateau, and COV would tend to a constant for further reduction in voxel size (2, 27). Surprisingly, the model data show instead a distinct decrease in COV as voxel size approaches that of the acinus. The dog data of Glenny et al. (27) included as an *inset* to Fig. 4 interestingly also shows a decrease in COV (labeled RD in that figure) with decreasing voxel size in the very smallest voxels analyzed for four of the six dogs considered (*dogs 1*, *2*, *3*, and *5*). In their study, Glenny et al. note that there is oscillation of observed COV about the regression line, and an oscillation is certainly apparent in our model data (most noticeably in the upright posture). This can be accounted for by the observation that the ideal sectioning of the lung to investigate fractal properties would be to group together regions of the lung that originate from the same branches of the vascular tree; it was suggested by Glenny et al. (27) that this type of grouping would reduce the magnitude of the oscillation. The apparent reduction of COV at small voxel sizes could possibly be accounted for, in the experimental study, as a result of this oscillation, or by a loss of resolution in imaging at a small spatial scale. However, it is sufficiently significant in modeling results that further discussion is warranted here. An alternate explanation for this reduction in COV at very small voxel sizes is that, at this scale, spatial correlation in perfusion (that originates predominantly due to gravitational influences rather than fractal properties of the system) becomes apparent.

It is well known that there is a spatial correlation in pulmonary perfusion, high-flow regions are likely to be near other high-flow regions, and, despite considerable heterogeneity within isogravitational planes, perfusion in dependent lung regions is typically higher than that in nondependent regions (22). If flow is truly random or purely fractal, then COV will increase with resolution, when flow is uniform COV will remain constant with resolution, and, when flow is spatially correlated, it is possible for COV to decrease with resolution (although this depends very much on the nature and strength of the spatial correlation). In terms of model results, it seems that the influence of gravity and shared upstream vessels on perfusion distribution acts to provide sufficient spatial correlation between flows for this reduction in COV at a small spatial scale to become evident. Of course, if the spatial scale was further refined to the point that perfusion was approximately uniform within a voxel, then COV would tend to a constant as expected. This does not mean that the structure of the model (or the human lung) below this spatial scale is not pseudofractal, but that the large-scale negative correlation between flows at points in the lung that are far from each other dominates in model solutions. If smaller samples of lung tissue were considered, for example, a region of interest in dependent, nondependent, or midlung, COV can still increase with resolution. This effect is far more apparent than expected in model data analysis and debatable when considering the existing experimental data. This is perhaps because the model data are noiseless, because of model artifacts, or may be due to structural simplifications required below the level of the acinus to satisfy computational constraints (use of a symmetric model for the acinus). However, it highlights the importance of spatial scale and gravitational influences on interpretation of COV in both modeling and image analysis, and that all measures of heterogeneity in pulmonary perfusion are estimates that must be interpreted carefully.

Perfusion gradients. Published measurements of perfusion gradients have a large variation in their range of values. Measured flow gradients are influenced by several factors, including intersubject variability (i.e., tissue properties, vascular structure, cardiac output, and pressures applied by the heart), the level of lung inflation, posture, and methods of image processing and analysis applied within the study (i.e., image resolution, edge exclusion criteria, etc.). Flow gradients from selected experimental studies in human lungs at FRC range from −2.1 to −11%/cm in the supine posture and −1.1 to −5.2%/cm in the prone posture (3, 35, 45, 46, 48). Our predicted values are reasonable given the range of values found in the literature, that our results were obtained with voxel and lung slice sizes that are considerably smaller than many used in the experimental literature, and that the model is applied in a single subject. As with COVs, per-voxel perfusion gradients

are scale dependent. For this subject, predicted perfusion gradients increase with voxel size up to a resolution of ~2.5-cm^3 voxels. Then, above this limit, as resolution becomes coarser, perfusion gradients begin to decrease with voxel size.

Computational modeling of perfusion distribution allows analysis of smaller spatial scales than imaging techniques enable: perfusion can be studied on a per-acinus basis rather than by averaging over voxels. It is well known that image resolution (and so the size of voxels considered) has an effect on the results of experimental studies. This effect is clearly also evident in the model perfusion gradients and heterogeneity. Figure 2*B* shows mean per-acinus flow rates in each posture. Density normalization was carried out in two ways: by dividing flow per voxel by the average ρ_t in that voxel (as predicted by our tissue mechanics model and validated against MDCT data), and by dividing flow per voxel by the number of acinar units in that voxel. Both methods improve agreement between the per-acinus and per-voxel cases in terms of predicted perfusion gradients, and, as voxel size decreases toward the size of an acinar unit, results begin to approach one another.

It is likely that, with development of model geometries representing normal subjects of various shapes and sizes, it will be possible to predict a range of values for predicted perfusion gradients that can be compared with literature values obtained using different classes of imaging techniques. Perfusion gradients were largest in the supine lung at FRC. There is a 14% decrease in the magnitude of the predicted perfusion gradient between the supine and prone postures; this compares to an ~26% decrease (48) and a 14% decrease (46) observed previously in experimental studies. Perfusion gradients increased with lung deflation and decreased with lung inflation (with inflation from FRC to TLC the perfusion gradient, using 1-cm^3 voxels, in the supine lung decreases by 25%), which is expected given the tendency toward more uniform distribution of lung ρ_t with inflation above FRC.

The influence of tissue deformation, vascular geometry, and hydrostatic effects. The advantage of this computational model over previous similar models is that it allows the relative influence of tissue deformation, vascular geometry, and the hydrostatic effects of gravity to be investigated within the full pulmonary circulation without the assumption of boundary conditions at the acinar level. Previous computational modeling of the relative influence of gravity and structure (9, 10, 13) considered perfusion in the arterial tree alone, with a linear (with respect to gravitational height) blood pressure distribution at the acinar level. This means that each acinus within a single isogravitational plane is assumed to have the same blood pressure. It was acknowledged in these studies that coupling isolated arterial and venous models with a model of capillary perfusion, and so a description of the relationship between P_A and blood pressure at the acinar level, would likely reveal a modified influence of gravity (10, 13). A major feature of pulmonary blood flow that is captured in this model (and not in previous models with a similar anatomically based structure) is a heterogeneous distribution of both absolute blood pressures at the acinar level and acinar driving pressures (Fig. 3). This distribution of pressures is influenced by tissue deformation, vascular geometry, and hydrostatic effects, making this complete circuit model a valuable tool in investigating the relative influence of each.

Postural differences: tissue deformation. The tissue mechanics model predicts a greater amount of tissue deformation in the supine posture than in the prone or upright postures, resulting in a larger perfusion gradient in the supine posture than in the other two postures (Table 1), which is consistent with experimental measurements (46, 48). Normalizing the flow values per voxel by the ρ_t in that voxel (all tissue, including blood as predicted by our tissue deformation model), or calculating flow on a per-acinus basis, provides flow per unit tissue and results in reduced perfusion gradients across all three postures. This normalization provides a correction for tissue deformation and results in flow gradients across the different lung volumes that are more comparable than flows per volume of tissue. This supports experimental studies that describe the lung tissue as acting as a Slinky that deforms under gravity (35, 48) and highlights the importance of normalizing perfusion by density.

If, in addition to density normalization, the region of reduced flow in dependent lung regions (zone 4) is omitted from calculations of perfusion gradients, it is clear that there is very little difference between gradients of perfusion between postures (Fig. 2*B*) in the model. This suggests that the orientation of the vascular structure with respect to gravity has little effect on perfusion gradients in the human lung (rather it affects perfusion heterogeneity) and that posture differences in perfusion gradients are largely due to tissue deformation. Importantly, even though postural differences can be accounted for by density normalization, a density normalized perfusion gradient is still evident.

The influence of vascular geometry (pathlength) on perfusion. Zone 4 is only predicted in theoretical models of pulmonary perfusion that include an asymmetric arterial structure, as all pathways to the acinus are the same in a symmetric structure. It has, therefore, been suggested that zone 4 occurs as a consequence of fluid dynamics in the preacinar arteries (11, 41, 57). The model predicts a reduction in flow in regions far from the feeding pulmonary arteries within isogravitational planes, and similarly zero-gravity simulations predict a region of reduced flow in regions far from the feeding pulmonary arteries in all directions, with reductions in mean flow of up to 20% in the basal region of the upright lung. Zero-gravity results are similar to those already presented in Burrowes et al. (9) (Fig. 3 in this paper), where perfusion was modeled in the arteries alone without tissue deformation. As the additional effect of tissue mechanics and "zonal" flow on solutions between models is not major in zero gravity results are not reproduced here. Our model also suggests that the pressure drop across an acinus is dependent on upstream resistance (Fig. 3). The reduction in flow in regions far from the feeding pulmonary arteries, together with the relationship between upstream resistance and acinar driving pressure, suggest that upstream resistance provides a significant contribution to pulmonary perfusion gradients.

The variation in pathlength and hence upstream resistance to the most dependent lung regions in prone, supine, and upright lungs is the likely contributing factor to the relative size of zone 4 in each posture, a finding that supports the recent experimental data of Hopkins et al. (34). In addition, the presence of reduced flow in distal arteries in zero gravity and within isogravitational planes suggests that long pathlengths in peripheral lung regions may also contribute to increase the magnitude of perfusion gradients. In addition, vascular geom-

etry is the largest contributor to perfusion heterogeneity, being responsible for a large proportion of the COV predicted by the model (Table 3). This means that multiple zones of flow can coexist in a single isogravitational slice. In the nondependent regions of the upright lung, the model predicts both zone 2 and zone 3 flow within isogravitational slices.

Hydrostatic effects. The hydrostatic effects of gravity are represented in the large blood vessels via the term $\rho_b\, gL\, \cos\Theta$ (*Eq. 3*), and by "zonal" flow in the capillary sheets. These hydrostatic effects introduce the gravitationally dependent gradient into pulmonary perfusion distributions, and, in the model, hydrostatic effects are the largest contributor to the perfusion gradient (Table 3). These gradients are substantially altered (at least in the human model) by the dual influence of tissue deformation and the geometry of the vasculature. Whether these influences act to increase or decrease observed perfusion gradients will vary between postures, individuals, and species. However, the importance of hydrostatic pressure in the development of pulmonary perfusion gradients should not be overlooked.

This study set out to address the following points: *1*) whether the hydrostatic pressure (within the blood only) makes a significant contribution to the pulmonary perfusion gradient in the human lung; *2*) whether tissue deformation is the major contribution of gravity to blood flow gradients; and *3*) whether the balance of pressures at the microcirculatory level remains a significant feature governing flow distribution in the presence of other mechanisms of gravitational origin. We conclude that, in the absence of tissue deformation, the hydrostatic effects of gravity on blood contribute to the establishment of the perfusion gradient and, in this model, to a substantial proportion of its magnitude. Hydrostatic effects (contributed via balances of pressures throughout the pulmonary circuit) produce the largest effect on flow gradients and outweigh the contribution of tissue deformation only slightly on a per-voxel basis, but substantially on a per-acinar basis (Table 3). Tissue deformation has a substantial effect on the magnitude of the perfusion gradient and is largely responsible for posture differences in perfusion gradients. The contribution of tissue deformation is more significant on a per-voxel than a per-acinar basis (Table 3), which would explain the differences found across experimental studies using either voxel-based imaging or "per tissue"-based microsphere measurements. The balance of pressures at the microcirculatory level is influenced by gravity, but also substantially by the vascular branching structure. This structure results in isogravitational heterogeneities in pulmonary perfusion and a reduction of flow in zone 4, indicating that the structure of the lung acts to alter the perfusion gradients that are introduced by the effects of gravity.

Model Limitations and Major Assumptions

Fung's sheet flow model relies on the geometric simplification that represents flow in the pulmonary microcirculation, as occurring between parallel plates, supported by posts of connective tissue, rather than representing the capillary bed as a network of branching tubules (29). This geometric and mathematical simplification results in a model of averaged flow in the capillary bed, which necessarily results in some loss in the detail of flow heterogeneity in the microcirculation. However, Fung's approach is based on a thorough fluid dynamic analysis, and the model is in general agreement with experimental data for flow and resistance across the pulmonary capillary bed. Our model also assumes a symmetric acinar branching structure, which may underestimate perfusion heterogeneity within the acinus. However, this simplification is necessary to couple the computationally expensive models describing perfusion in anatomically realistic large arterial and venous vessels.

Our model assumes each acinus to consist of nine generations each of arterioles and venules. Although this is typical of an acinus in the human lung (30), it may result in an underestimation of perfusion heterogeneity. To test the effect of heterogeneity in acinar size, we repeated our simulations in the supine lung at FRC with a randomly allocated number of acinar blood vessel generations between 6 and 12. For each acinus, a pseudorandom number between 0 and 1 was generated from a uniform distribution. Then the range of numbers 0–1 was divided into 7 equal ranges (one for each generation between 6 and 12), and the number of acinar blood vessel generations was assigned based on the size of the generated pseudorandom number. This resulted in a change in PVR of just 0.16% and a slight increase in COV (36.2% on the per-acinus basis compared with 34.6%). This suggests that heterogeneity in (whole lung) perfusion is more greatly influenced by heterogeneity in the large blood vessel structure than the small-vessel structure, which goes some way toward justifying this modeling assumption.

A steady laminar blood flow is assumed in the lung, and possible additional energy dissipation at vessel bifurcations is not considered. Turbulent flow is unlikely to occur in any but the largest pulmonary blood vessels, as Reynolds numbers in these vessels are generally sufficiently small. This study focuses on the distribution of flow through the lung, and information gained from simplified flow equations is sufficient to provide important information regarding this distribution. Although some models of perfusion in the lung consider pulsatile flow (38, 61), most consider steady flow (6, 11, 42, 62), and this approach is considered to be appropriate in studies of PVR and perfusion distribution (15).

The modeling techniques described here allow subject-specific models to be developed to compare perfusion between subjects. However, data availability means that there are currently limitations to the extent that this can be achieved. Where subject-specific data are not available, for example, in defining unstressed vessel radii, previously published experimental data must be used in place of subject-specific data. The available morphometric data sets providing $R_D S$ values and vessel radii are limited to a small number of subjects and do not necessarily correspond to the size, sex, or body composition of a particular subject. Some of these parameters are hence used as fit parameters in the model, with fitted values falling within measured ranges. In addition, some vessel orientations are based on airway rather than blood vessels (although the airway tree is segmented from the same subject, and, on the scale that this assumption was made, blood vessels follow airways closely). With advancements in imaging resolution and blood vessel segmentation providing more detailed subject-specific data in the future, the predictive power of this model and the potential for intersubject comparisons will presumably become greater. However, the detailed parameter sensitivity analysis given in Table 2 provides an indication of how deviations from assumed parameters affect perfusion measures.

We rely on supine CT data to construct model geometries and assume that tissue is uniformly distributed at TLC in the supine posture. Given that TLC volumes in the upright posture are generally larger than in the supine posture, this assumption may be inaccurate. However, without imaging available for the upright posture (where the lung tissue is theoretically most uniformly expanded), the assumption is necessary. In addition, the model does not include geometry changes due the movement of the chest wall, diaphragm, or heart with posture. Including these geometry changes may further improve the PVRs and perfusion gradients predicted in each posture. Some studies in humans and primates have suggested a larger perfusion gradient in the upright posture than in the supine or prone postures (1, 4, 23, 44, 58). Our model predicts the smallest gradient in the upright human due to a comparatively large zone 4 in this posture. When zone 4 regions are neglected (as is the case in several of these experimental studies), the gradients in each posture are similar, but the upright gradient is not largest. The reason for this discrepancy with experimental data is unclear, but may be due to the reliance on supine CT data to construct model geometries.

Conclusion

We have developed an integrated multiscale model that can reveal insights into the function of the pulmonary circulation that are difficult to attain experimentally or theoretically by studying only the isolated components of the system. The model supports previous experimental studies that demonstrate the importance of tissue deformation in establishing gravitational gradients of perfusion, and, in addition, it demonstrates that the hydrostatic pressure gradient makes a significant posture-independent contribution to the perfusion gradient. The present analysis shows that posture differences in perfusion gradients can be explained as a result of the combined effect of tissue deformation and the relative size of zone 4, which is a region of reduced flow in the most gravitationally dependent lung regions. The coupling of large- and small-scale models reveals significant variation in the microcirculatory driving pressure within isogravitational planes, which is a consequence of heterogeneous large-vessel resistance and is amplified by the complex balance of capillary pressures, distension, and flow, which arise from the traditional zonal model and its description of the link between these microcirculatory properties. An interesting point that merits further experimental and modeling study is the apparent oscillation of the COV (or RD coefficient) about its line of regression against voxel size that is perhaps indicative of spatial correlation in perfusion that is nonfractal in origin.

APPENDIX

Per-voxel Analysis of Model Data Including All Vessels

The per-voxel analysis presented in the main text of this paper includes summed flows in each voxel, but includes only acinar blood vessels. This analysis technique aims to mimic imaging measures using radiolabeled macroaggregates that become lodged in parenchymal tissue (46). Other imaging techniques, such as functional MRI (48), cannot distinguish between intra- and extra-acinar blood vessels. Therefore, a per-voxel analysis was carried out that included all blood vessels, except the largest central blood vessels.

For this analysis technique, the lung was divided into a number of equally sized cubes (or voxels). Defining the blood flow per vessel as the flow rate at each bifurcation point, flow to all vessels within each voxel was summed before calculation of gradients and COVs. Vessels were excluded from analysis if the flow rate in that vessel was more than four times the overall mean flow (the total flow through the lung divided by the number of blood vessels). Voxels were omitted from analysis if they lay on the surface of the lung and were only partially filled with lung tissue (edges were excluded). If a finite element representing an acinus lies on the boundary between voxels, it is assigned to only one of the voxels.

Gradients of blood flow with respect to gravitational height were calculated using a linear regression analysis and, in the case of 1-cm^3 voxels, were found to be -11.3%/cm ($R^2 = 0.42$), -9.82%/cm ($R^2 = 0.34$), and -5.20%/cm ($R^2 = 0.24$) in the supine, prone, and upright postures, respectively. These gradients differ only slightly from those given in Table 1 (*column 4*) that are calculated on a per-voxel basis but include only acinar blood vessels. The COVs (overall standard deviation divided by the mean flow per voxel) were calculated to be 66.6, 63.3, and 55.0% in the supine, prone, and upright postures, respectively. These COVs are slightly higher than those calculated on a per-voxel basis, but, with acini only included in analysis, are quite consistent with the results of that analysis technique.

GRANTS

This work was supported by National Heart, Lung, and Blood Institute Grant R01-HL-064368 (E. A. Hoffman), and Health Research Council of New Zealand grant 09/143 (M. H. Tawhai). K. S. Burrowes was supported by an Engineering and Physical Sciences Research Council Postdoctoral Fellowship at the Life Sciences Interface.

DISCLOSURES

No conflicts of interest, financial or otherwise, are declared by the author(s).

REFERENCES

1. **Amis TC, Jones HA, Hughes JM.** Effect of posture on inter-regional distribution of pulmonary perfusion and VA/Q ratios in man. *Respir Physiol* 56: 169–182, 1984.
2. **Bassingthwaighte JB.** Physiological heterogeneity: fractals link determinism and randomness in structures and functions. *News Physiol Sci* 3: 5–10, 1988.
3. **Brudin LH, Rhodes CG, Valind SO, Jones T, Hughes JMB.** Interrelationships between regional blood flow, blood volume, and ventilation in supine humans. *J Appl Physiol* 76: 1205–1210, 1994.
4. **Bryan AC, Bentivolgio LG, Beerel F, MacLeish H, Zidulka A, Bates DV.** Factors affecting regional distribution of ventilation and perfusion in the lung. *J Appl Physiol* 19: 395–402, 1964.
5. **Bshouty Z, Younes M.** Distensibility and pressure-flow relationship of the pulmonary circulation. I. Single-vessel model. *J Appl Physiol* 68: 1501–1513, 1990.
6. **Bshouty Z, Younes M.** Distensibility and pressure-flow relationship of the pulmonary circulation. II. Multibranched model. *J Appl Physiol* 68: 1514–1527, 1990.
7. **Burrowes KS, Hoffman EA, Tawhai MH.** Species-specific pulmonary arterial asymmetry determines species differences in regional pulmonary perfusion. *Ann Biomed Eng* 37: 2497–2509, 2009.
8. **Burrowes KS, Hunter PJ, Tawhai MH.** Anatomically-based finite element models of the human pulmonary arterial and venous trees including supernumerary vessels. *J Appl Physiol* 99: 731–738, 2005.
9. **Burrowes KS, Hunter PJ, Tawhai MH.** Evaluation of the effect of postural and gravitational variations on the distribution of pulmonary blood flow via an image-based computational model. In: *Conf Proc IEEE Eng Med Biol Soc 27th Annual Conference*. Shanghai, China: IEEE Engineering in Medicine and Biology Society, 2005, p. 6138–6140.
10. **Burrowes KS, Hunter PJ, Tawhai MH.** Investigation of the relative effects of vascular branching structure and gravity on pulmonary arterial blood flow heterogeneity via an image-based computational model. *Acad Radiol* 12: 1464–1474, 2005.
11. **Burrowes KS, Tawhai MH.** Computational predictions of pulmonary blood flow gradients: gravity versus structure. *Respir Physiol Neurobiol* 154: 515–523, 2006.

12. **Burrowes KS, Tawhai MH, Hunter PJ.** Modeling RBC and neutrophil distribution through an anatomically based pulmonary capillary network. *Ann Biomed Eng* 32: 585–595, 2004.
13. **Burrowes KS, Tawhai MT.** Coupling of lung tissue tethering force to fluid dynamics in the pulmonary circulation. *Int J Numerical Methods Biomed Eng* 26: 862–875, 2010.
14. **Clark AR, Burrowes KS, Tawhai MT.** Contribution of serial and parallel micro-perfusion to spatial variability in pulmonary inter- and intra-acinar blood flow. *J Appl Physiol* 108: 1116–1126, 2010.
15. **Clough AV, Audi SH, Molthen RC, Krenz GS.** Lung circulation modeling: status and prospect. *Proc IEEE* 94: 753–768, 2006.
16. **Fung YC.** *Biomechanics: Circulation.* New York: Springer Verlag, 1997.
17. **Fung YC, Sobin SS.** Elasticity of the pulmonary alveolar sheet. *Circ Res* 30: 451–469, 1972.
18. **Fung YC, Sobin SS.** Theory of sheet flow in lung alveoli. *J Appl Physiol* 26: 472–488, 1969.
19. **Fung YC, Yen RT.** A new theory of pulmonary blood flow in zone 2 condition. *J Appl Physiol* 60: 1638–1650, 1986.
20. **Gehr P, Bachofen M, Weibel ER.** The normal human lung: ultrastructure and morphometric estimation of diffusion capacity. *Respir Physiol* 32: 121–140, 1978.
21. **Glazier JB, Hughes JMB, Maloney JE, West JB.** Measurements of capillary dimensions and blood volume in rapidly frozen lungs. *J Appl Physiol* 26: 65–76, 1969.
22. **Glenny RW.** Spatial correlation of regional pulmonary perfusion. *J Appl Physiol* 72: 2378–2386, 1992.
23. **Glenny RW, Bernard S, Robertson HT, Hlastala MP.** Gravity is an important but secondary determinant of regional pulmonary blood flow in upright primates. *J Appl Physiol* 86: 623–632, 1999.
24. **Glenny RW, Bernard SL, Robertson HT.** Pulmonary blood remains fractal down to the level of gas exchange. *J Appl Physiol* 89: 742–748, 2000.
25. **Glenny RW, Lamm WJE, Albert RK, Robertson HT.** Gravity is a minor determinant of pulmonary blood flow distribution. *J Appl Physiol* 71: 620–629, 1991.
26. **Glenny RW, Robertson TJ.** Fractal properties of pulmonary blood flow: characterization of spatial heterogeneity. *J Appl Physiol* 69: 532–545, 1990.
27. **Glenny RW, Robertson HT, Yamashiro S, Bassingthwaighte JB.** Applications of fractal analysis to physiology. *J Appl Physiol* 70: 2351–2367, 1991.
28. **Godbey PS, Graham JA, Presson RG Jr, Wagner WW Jr, Lloyd TC Jr.** Effect of capillary pressure and lung distension on capillary recruitment. *J Appl Physiol* 79: 1142–1147, 1995.
29. **Guntheroth WG, Luchtel DL, Kawabori I.** Pulmonary microcirculation: tubules rather than sheet or post. *J Appl Physiol* 53: 510–515, 1982.
30. **Haefeli-Bleuer B, Weibel ER.** Morphometry of the human pulmonary acinus. *Anat Rec* 220: 401–414, 1988.
31. **Hlastala MP, Glenny RW.** Vascular structure determines pulmonary blood flow distribution. *News Physiol Sci* 14: 182–186, 1999.
32. **Hoffman EA, Clough AV, Christensen GE, Lin CL, McLennan G, Reinhardt JM, Simon BA, Sonka M, Tawhai MH, van Beek EJ, Wang G.** The comprehensive imaging-based analysis of the lung: a forum for team science. *Acad Radiol* 11: 1370–1380, 2004.
33. **Hoffman EA, Reinhardt JM, Sonka M, Simon BA, Guo J, Saba O, Chon D, Samrah S, Shikata H, Tschirren J, Palagyi K, Beck KC, McLennan G.** Characterization of the interstitial lung diseases via density-based and texture-based analysis of computed tomography images of lung structure and function. *Acad Radiol* 10: 1104–1118, 2003.
34. **Hopkins SR, Arai TJ, Henderson AC, Levin DL, Buxton RB, Prisk GK.** Lung volume does not alter the distribution of pulmonary perfusion in dependent lung in supine humans. *J Physiol* 588: 4759–4768, 2010.
35. **Hopkins SR, Henderson AC, Levin DL, Yamada K, Arai T, Buxton RB, Prisk GK.** Vertical gradients in regional lung density and perfusion in the supine human lung: the Slinky effect. *J Appl Physiol* 103: 240–248, 2007.
36. **Horsfield K, Gordon WI.** Morphometry of pulmonary veins in man. *Lung* 159: 211–218, 1981.
37. **Howell JBL, Permutt S, Proctor DF, Riley RL.** Effect of inflation of the lung on different parts of the pulmonary vascular bed. *J Appl Physiol* 16: 71–76, 1961.
38. **Huang W, Tian Y, Gao J, Yen RT.** Comparison of theory and experiment in pulsatile flow in cat lung. *Ann Biomed Eng* 26: 812–820, 1998.
39. **Huang W, Yen RT, McLaurine M, Bledsoe G.** Morphometry of the human pulmonary vasculature. *J Appl Physiol* 81: 2123–2133, 1996.
40. **Huang Y, Doerschuk CM, Kamm RD.** Computational modeling of RBC and neutrophil transit through the pulmonary capillaries. *J Appl Physiol* 90: 545–564, 2001.
41. **Hughes JMB, Glazier JB, Maloney JE, West JB.** Effect of extra-alveolar vessels on distribution of blood flow in the dog lung. *J Appl Physiol* 25: 701–712, 1968.
42. **Krenz GS, Dawson CA.** Flow and pressure distributions in vascular networks consisting of distensible vessels. *Am J Respir Crit Care Med* 284: H2192–H2203, 2003.
43. **Levitsky MG.** *Pulmonary Physiology.* New York: McGraw-Hill, 1991.
44. **Maeda H, Itoh H, Ishii Y, Todo G, Mukai T, Fujita M, Kambara H, Kawai C, Torizuka K.** Pulmonary blood flow distribution measured by radionuclide-computed tomography. *J Appl Physiol* 54: 225–233, 1983.
45. **Musch G, Layfield JDH, Harris RS, Melo MFV, Winkler T, Callahan RJ, Fischman AJ, Venegas JG.** Topographical distribution of pulmonary perfusion and ventilation, assessed by PET in supine and prone humans. *J Appl Physiol* 93: 1841–1851, 2002.
46. **Petersson J, Rohdin M, Sanchez-Crespo A, Nyren S, Jacobsson H, Larsson SA, Lindahl SGE, Linnarsson D, Neradilek B, Polissar NL, Glenny RW, Mure M.** Posture primarily affects lung tissue distribution with minor effect on blood flow and ventilation. *Respir Physiol Neurobiol* 156: 293–303, 2007.
47. **Pries AR, Secomb TW, Gaehtgens P.** Biophysical aspects of blood flow in the microvasculature. *Cardiovasc Res* 32: 654–667, 1996.
48. **Prisk GK, Yamada K, Henderson AC, Arai TJ, Levin DL, Buxton RB, Hopkins SR.** Pulmonary perfusion in the prone and supine postures in the normal human lung. *J Appl Physiol* 103: 883–894, 2007.
49. **Rodriguez-Roisin R, Krowka MJ, Herve PH, Fallon MB.** Pulmonary-hepatic vascular disorders. *Eur Respir J* 24: 861–880, 2004.
50. **Singhal S, Henderson R, Horsfield K, Harding K, Cumming G.** Morphometry of the human pulmonary arterial tree. *Circ Res* 33: 190–197, 1973.
51. **Sobin SS, Tremer HM, Lindal RG, Fung YC.** Distensibility of human pulmonary capillary blood vessels in the interalveolar septa (Abstract). *Federation Proc* 38: 990, 1979.
52. **Tawhai MH, Hunter PJ, Tschirren J, Reinhardt JM, McLennan G, Hoffman EA.** CT-based geometry analysis and finite element models of the human and ovine bronchial tree. *J Appl Physiol* 97: 2310–2321, 2004.
53. **Tawhai MH, Nash MP, Lin CL, Hoffman EA.** Supine and prone differences in regional lung density and pleural pressure gradients in the human lung with constant shape. *J Appl Physiol* 107: 912–920, 2009.
54. **Thomas LJ, Griffo ZJ, Roos A.** Effect of negative pressure inflation of the lung on pulmonary vascular resistance. *J Appl Physiol* 16: 451–456, 1961.
55. **Wagner WW, Presson RG.** Complexity of perfusion in the pulmonary gas exchange vessels. In: *Complexity in Structure and Function of the Lung*, edited by Hlastala MP and Robertson HT. New York: Dekker, 1998, p. ?-?.
56. **Weibel ER.** *The Pathway for Oxygen: Structure and Function in the Mammalian Respiratory System.* Cambridge, MA: Harvard University Press, 1984.
57. **West JB.** Distribution of pulmonary blood flow. *Am J Crit Care* 160: 1802–1803, 1999.
58. **West JB, Dollery CT.** Distribution of blood flow and ventilation-perfusion ratio in the lung, measured with radioactive carbon dioxide. *J Appl Physiol* 15: 405–410, 1960.
59. **West JB, Dollery CT, Naimark A.** Distribution of blood flow in isolated lung; relation to vascular and alveolar pressures. *J Appl Physiol* 19: 713–724, 1964.
60. **Yen RT, Fung YC, Bingham N.** Elasticity of small pulmonary arteries in the cat. *J Biomech Eng* 102: 170–177, 1980.
61. **Zhou Q, Gao J, Huang W, Yen M.** Vascular impedance analysis in human pulmonary circulation. *Biomed Sci Instrum* 42: 470–475, 2006.
62. **Zhuang FY, Fung YC, Yen RT.** Analysis of blood flow in cat's lung with detailed anatomical and elasticity data. *J Appl Physiol* 55: 1341–1348, 1983.